NASA/TP–2015-218986

Flexible Micropost Arrays for Shear Stress Measurement

Christopher J. Wohl, Frank L. Palmieri, John W. Hopkins,
Allen M. Jackson, and John W. Connell
Langley Research Center, Hampton, Virginia

Yi Lin
National Institute of Aerospace, Hampton, Virginia

Alexxandra A. Cisotto
Langley Research Center Hampton, Virginia

December 2015

NASA STI Program . . . in Profile

Since its founding, NASA has been dedicated to the advancement of aeronautics and space science. The NASA scientific and technical information (STI) program plays a key part in helping NASA maintain this important role.

The NASA STI program operates under the auspices of the Agency Chief Information Officer. It collects, organizes, provides for archiving, and disseminates NASA's STI. The NASA STI program provides access to the NTRS Registered and its public interface, the NASA Technical Reports Server, thus providing one of the largest collections of aeronautical and space science STI in the world. Results are published in both non-NASA channels and by NASA in the NASA STI Report Series, which includes the following report types:

- TECHNICAL PUBLICATION. Reports of completed research or a major significant phase of research that present the results of NASA Programs and include extensive data or theoretical analysis. Includes compilations of significant scientific and technical data and information deemed to be of continuing reference value. NASA counter-part of peer-reviewed formal professional papers but has less stringent limitations on manuscript length and extent of graphic presentations.

- TECHNICAL MEMORANDUM. Scientific and technical findings that are preliminary or of specialized interest, e.g., quick release reports, working papers, and bibliographies that contain minimal annotation. Does not contain extensive analysis.

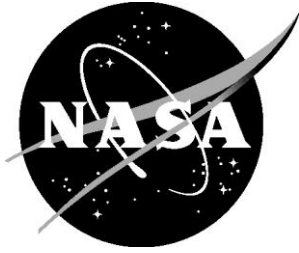- CONTRACTOR REPORT. Scientific and technical findings by NASA-sponsored contractors and grantees.

- CONFERENCE PUBLICATION. Collected papers from scientific and technical conferences, symposia, seminars, or other meetings sponsored or co-sponsored by NASA.

- SPECIAL PUBLICATION. Scientific, technical, or historical information from NASA programs, projects, and missions, often concerned with subjects having substantial public interest.

- TECHNICAL TRANSLATION. English-language translations of foreign scientific and technical material pertinent to NASA's mission.

Specialized services also include organizing and publishing research results, distributing specialized research announcements and feeds, providing information desk and personal search support, and enabling data exchange services.

For more information about the NASA STI program, see the following:

- Access the NASA STI program home page at http://www.sti.nasa.gov

- E-mail your question to help@sti.nasa.gov

- Phone the NASA STI Information Desk at 757-864-9658

- Write to:
  NASA STI Information Desk
  Mail Stop 148
  NASA Langley Research Center
  Hampton, VA 23681-2199

NASA/TP–2015-218986

Flexible Micropost Arrays for Shear Stress Measurement

Christopher J. Wohl, Frank L. Palmieri, John W. Hopkins,
Allen M. Jackson, and John W. Connell
Langley Research Center, Hampton, Virginia

Yi Lin
National Institute of Aerospace, Hampton, Virginia

Alexxandra A. Cisotto
Langley Research Center Hampton, Virginia

December 2015

Acknowledgment

Available from:

NASA STI Program / Mail Stop 148
NASA Langley Research Center
Hampton, VA 23681-2199
Fax: 757-864-6500

Abstract

Increased fuel costs, heightened environmental protection requirements, and noise abatement continue to place drag reduction at the forefront of aerospace research priorities. Unfortunately, shortfalls still exist in the fundamental understanding of boundary-layer airflow over aerodynamic surfaces, especially regarding drag arising from skin friction. For example, there is insufficient availability of instrumentation to adequately characterize complex flows with strong pressure gradients, heat transfer, wall mass flux, three-dimensionality, separation, shock waves, and transient phenomena. One example is the acoustic liner efficacy on aircraft engine nacelle walls. Active measurement of shear stress in boundary layer airflow would enable a better understanding of how aircraft structure and flight dynamics affect skin friction.

Current shear stress measurement techniques suffer from reliability, complexity, and airflow disruption, thereby compromising resultant shear stress data. The state-of-the-art for shear stress sensing uses indirect or direct measurement techniques. Indirect measurements (e.g., hot-wire, heat flux gages, oil interferometry, laser Doppler anemometry, small scale pressure drag surfaces, i.e., fences) require intricate knowledge of the studied flow, restrictive instrument arrangements, large surface areas, flow disruption, or seeding material; with smaller, higher bandwidth probes under development. Direct measurements involve strain displacement of a sensor element and require no prior knowledge of the flow. Unfortunately, conventional "floating" recessed components for direct measurements are mm to cm in size. Whispering gallery mode devices and Fiber Bragg Gratings are examples of recent additions to this type of sensor with much smaller (μm) sensor components. Direct detection techniques are often single point measurements and difficult to calibrate and implement in wind tunnel experiments. In addition, the wiring, packaging, and installation of delicate micro-electromechanical devices impede the use of most direct shear sensors. Similarly, the cavity required for sensing element displacement is sensitive to particulate obstruction.

This work was focused on developing a shear stress sensor for use in subsonic wind tunnel test facilities applicable to an array of test configurations. The non-displacement shear sensors described here have minimal packaging requirements resulting in minimal or no disturbance of boundary layer flow. Compared to previous concepts, device installation could be simple with reduced cost and down-time. The novelty lies in the creation of low profile (nanoscale to 100 μm) micropost arrays that stay within the viscous sub-layer of the airflow. Aerodynamic forces, which are related to the surface shear stress, cause post deflection and optical property changes.

Ultimately, a reliable, accurate shear stress sensor that does not disrupt the airflow has the potential to provide high value data for flow physics researchers, aerodynamicists, and aircraft manufacturers leading to greater flight efficiency arising from more in-depth knowledge on how aircraft design impacts near surface properties.

Table of Contents

Table of Figures

Table of Tables

Nomenclature

Acronyms

AFM...........................atomic force microscopy

MEMS........................microelectromechanical systems

PGMEA......................propylene glycol monomethyl ether acetate

μ-PIV ....micro particle image velocimetry

Symbols

A..................................area

c_D.................................drag coefficient

D.................................diameter

E.................................Elastic modulus

I..................................area moment of inertia

L.................................micropost length

mPa............................millipascals

MPa............................megapascals

P.................................load

$Re\ (R)$.........................Reynold's number

v..................................velocity

y..................................post length

μm ....micrometers

τ..................................shear force

ρ..................................density

Section 1. **Introduction**

The utility of high aspect ratio structures as environmental sensors has been observed in nature with a variety of functions including tactile sensing, motion, noise, electrical signals, etc. Researchers have fabricated artificial devices to emulate the efficacy and sensitivity of these natural systems (Ref. 1). By natural extension, researchers have investigated the use of these high aspect ratio structures for the measurement of shear forces. State-of-the-art shear stress measurement techniques are often encumbered by the lack of precision, environmental sensitivity, and implementation complexity. In some cases, these sensors require extensive knowledge of the airflow, as they directly interfere with the experimental results. Naughton and Sheplak (Ref. 2) and Lofdahl and Gad-El Hak (Ref. 3) have recently reviewed the state-of-the-art for shear stress sensing in wind tunnels. To overcome these challenges, advanced microelectromechanical systems (MEMS) (Ref. 4) and other promising techniques, including whispering gallery mode sensors (Ref. 5) and micropost array devices (Ref. 6), are currently being explored.

Brücker, Große, and Schröder have extensively investigated the application of micropost arrays for shear stress sensing in fluid flows (Ref. 7). In their work, microposts were fabricated via soft lithography from a wax mold template which was patterned using laser ablation (Ref. 8). With 300–500 μm tall posts, they demonstrated deflection of the posts in fluid flows that were visualized using micro particle image velocimetry (μ-PIV) measurements (Ref. 7). The deflection of the posts was calibrated utilizing a plate and cone rheometer where the experimentally determined deflection was found to correlate well with theoretical calculations. They also evaluated micropost frequency response and demonstrated the ability to measure both mean (Ref. 9) and dynamic (Ref. 10) wall shear stress measurements for water flowing through a circular pipe. Very recently, their micropost arrays were utilized in a wind tunnel to measure shear stress and although there were issues with resonance complications at higher Reynolds numbers, the results indicated that micropost arrays are amenable to wind tunnel measurements of shear stress (Ref. 11).

Several techniques have been demonstrated to efficaciously fabricate high aspect ratio structures. Other applications for these structures, including adhesive free pressure sensitive adherent based on Gecko toe topographies (Ref. 12, 13) and fabrication of superhydrophobic surfaces (Ref. 14), have contributed to the rapid development of these fabrication techniques. The most widely used method to generate micropost structures has been contact lithography followed by plasma etching (Ref. 15, 16) or soft lithography (Ref. 17). Laser ablation patterning to generate templates for soft lithography fabrication has also been demonstrated (Ref. 6, 18). Using this approach, structures with aspect ratios (length/diameter) greater than 10 have been fabricated. More exotic methods, such as growth of nanowire forests and unique tooling were also shown to be effective for generating shear sensing posted surfaces (Ref. 19, 20). With such extensive use of these high aspect ratio structures, researchers recently identified requirements for rigidity and post spacing (Ref. 21) to resist collapse due to adhesive and capillary forces. The buckling strength of microposts, derived from beam theory, has also been investigated (Ref. 6). Based on the target post dimensions and post density for the surfaces fabricated here, it is not anticipated that buckling or collapse will be an issue.

In this work, micropost arrays were generated via soft lithography from templates. The reusable templates were fabricated using either laser ablation patterning or contact lithography and

enabled posts with aspect ratios up to 4 to be reliably produced. The microposts were fabricated from several silicones with varying mechanical properties and post deflection was characterized using atomic force microscopy. Thin "caps" were generated on the tops of the microposts to be used as aids for deflection-sensing. A macroscopic post array, for visualization and demonstration purposes, was fabricated and post-deflection in a bench top wind tunnel was recorded using high speed photography.

Section 2. **Preliminary Design Considerations**

Several factors were considered in determining the height of the microposts, the spacing of the microposts in the array, and their mechanical properties. For the development of this sensor, flow properties will be limited to developed subsonic turbulent flows with a Reynolds number, *Re*, greater than 5×10^5. The microposts should not extend beyond 5 viscous wall units to remain within the viscous sublayer, or approximately 100 micrometers (μm) for typical low speed wind tunnel laboratory flows. Posts should be spaced at least four times the diameter of the post "cap" (see description of post capping below) in order to prevent interference between adjacent posts and a cumulative disruption of the airflow properties, for example by a wake shed from an upstream post that would disrupt the airflow of any downstream posts that are too close.

It was decided to target a maximum deflection of 10 percent of the beam length such that the beam dynamics could be described by classic Euler-Bernoulli beam theory. The force imparted on a post in a flow is distributed over the post surface and should vary non-linearly from base to tip due to microscopic velocity gradients in the boundary layer. A simplifying assumption was made to estimate post deflection by placing the total bending load at the post tip. Other models such as linear load gradients along the length of the post did not have a significant impact on the calculation result. The deflection at the tip of a post, *y*, arising from all forces including form drag and skin friction can be calculated according to:

$$y = \frac{PL^3}{3EI}$$

(1)

where *L* is the post length, *E* is the elastic modulus, *P* is the load, and *I* is the area moment of inertia, which in this work was approximated as a rectangle with a fixed base ($I=1/3bL^3$). This expression assumes that the total bending load is at the post tip. Other models, including distribution of the load along the pillar length, did not significantly impact the calculated results. The load can be described as $P=D$, where *D* is the profile drag, $D=1/2\rho v^2 S c_D$, and c_D is the drag coefficient. Thus, Eq. 1 can be rewritten for the sensing elements described in this work by approximating the features as a cylinder with a rectangular face as the frontal area, $S=L2r$, where *r* is the pillar radius, which results in a c_D of 1. Rearranging this equation to determine the requisite elastic modulus of the micropost material yields:

$$E = \frac{4\rho v^2 L c_D}{3\pi r^3 Y}$$

(2)

Based on these considerations, calculations were performed to characterize a micropost 100 μm in length and 10 μm in radius, *r*, and with an elastic modulus of 0.15 MPa (the typical elastic modulus of silicones varies from 0.1–3.0 MPa). Such a post would undergo deflections of approximately 10 percent of the post length when exposed to a profile drag of 35.5 nN (figure 1), which correlates to a freestream velocity of approximately 12 m/s (see Appendix A). Given a resolution capability of 100 nm, which is lower than the state-of-the-art (see section 3.5), the minimal velocity requisite to detectably deflect such a post was approximately 0.6 m/s.

Although smaller posts would create fewer disturbances in the flow being measured, fabricating posts with radii less than 10 micrometers was beyond the capabilities of the available facilities. In addition, optical resolution needed for detection of post displacement is limited; therefore,

3

smaller posts would suffer from reduced sensitivity. Thus, micropost geometries were determined to be of greatest applicability with $L \leq 100$ µm, aspect ratios $(L/2r) \geq 5$, post spacing of four times the post "cap," and were to be comprised of elastomeric materials with an elastic modulus of ≤ 3 MPa. Other forces can play a role in post deflection including pressure drag, lift forces normal to the flow vector, inertial forces, and normal pressure forces (Ref. 22). It is expected that these sensors will have to be calibrated in a known flow field. Additionally, the mechanical properties of a silicone material, like most materials, are temperature sensitive. The relationship between mechanical properties and temperature is well characterized for these materials and can be accounted for using concurrent temperature measurement.(Ref. 23) Creep and thermal aging may also change the response of the posts but has not been considered and are likely to be negligible considering the expected lifetime of a sensor, approximately 1 year.
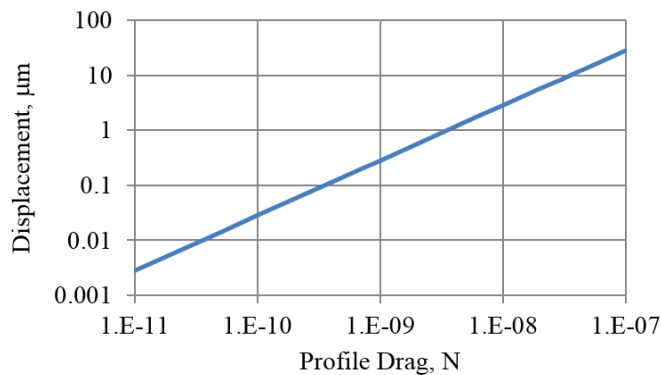

Figure 1. Calculated drag-displacement curve for a hypothetical post 100 µm in length and 10 µm in radius. The hypothetical post had an elastic modulus of 0.15 MPa.

Section 3. **Template Fabrication Experiments**

3.1 **Laser Ablation Patterning**

3.1.1 *Material Choice*

Based on the researchers' experience with laser ablation (Ref. 24, 25), it was determined that a polymeric material would be best for use as the master template. A common and readily available two-part epoxy was investigated as an ablation medium comprised of D.E.R. 331 (Dow) and Ethacure 100 (Albemarle Corporation).

Controlling the thickness and planarity of the epoxy is significant to control the ultimate post heights. Several techniques were employed to address the issue of the epoxy "de-wetting" the silica surface after it was spin-cast. Surface oxidation and utilization of adhesion-promoting surface chemical modifiers were investigated with moderate success. A molding technique that has successfully demonstrated control over bondline thickness in adhesion bonding experiments was utilized with significant improvements in surface wetting and epoxy thickness. For this, a glass plate was prepared by solvent cleaning and a small aliquot of the uncured epoxy mixture was placed in the middle of the plate. This was surrounded by aluminum alloy shim stock (76.2 μm thick) and the entire surface was covered with a sheet of polytetrafluoroethylene and another glass plate. This assembly was placed in a vacuum bag to spread the epoxy. The vacuum was then removed and weights were placed on the assembly to maintain flatness and keep the epoxy level over a 24-h period at ambient temperature. Next, the assembly and weights were placed in a convection oven and stage heated over the course of 72 h to an ultimate cure temperature of 175 °C. This was performed to enable partial curing of the epoxy at low temperatures resulting in controlled increase in viscosity. Through this process, epoxy-coated glass plates have been prepared that are more planar and have a uniform and consistent thickness of approximately 75 μm.

Another approach to overcome issues with de-wetting of the epoxy on the substrate would be to use an epoxy that cures more rapidly. Along those lines, a 30 minute cure epoxy (Great Plains 30 Minute Pro Epoxy) was utilized to make a series of glass-coated samples. These samples were prepared by placing a small volume (approximately 3 mL) of the mixed two-part epoxy onto the center of a glass disk that was placed on the spin coater. Several samples were prepared at different spin speeds with a constant duration (60 s) to develop a spin thickness curve (figure 2).
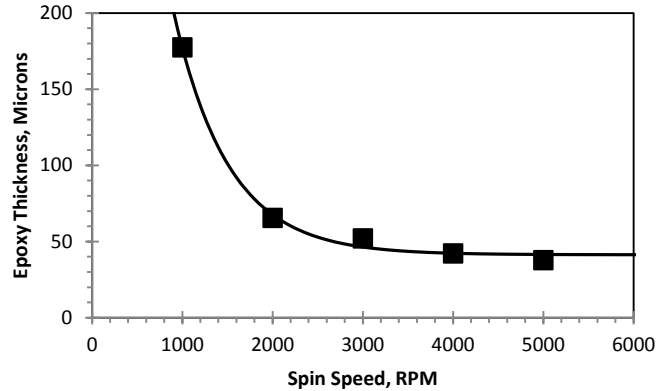
Figure 2. Spin curve developed for the 30 minute cure epoxy deposited on glass slides. The square dots are the data points and the solid line is an exponential fit. The correlation coefficient for this fit was > 0.99.

Using the spin curve in figure 2, 120 µm thick epoxy-coated glass disks were generated using both a single deposition step and two deposition steps. For the two step deposition process, an initial layer of the epoxy was spin-coated onto the glass disk and placed in a warming oven (70 °C) for 1 hour. This process was repeated to deposit a second epoxy layer on top of the first one. Using the two step process, epoxy thickness variability was reduced from sample to sample relative to the single deposition step process.

3.1.2 *Laser Technique*

Initially, the laser ablation process involved tracing a small circular area (25.4 µm) on the ablated material. Since the beam diameter is approximately 20 µm, this resulted in features that were 30–40 µm. In an effort to further reduce the feature diameter, a "drill" technique was evaluated. In this technique, instead of having the laser beam translated along a region, the position of the laser beam was fixed and a discrete number of pulses was delivered to the surface. Using this laser drilling approach, the diameters were reduced to approximately 20–30 µm.

Ablation of the epoxy worked well; the middle portion of the ablation profile had fairly uniform thickness with nearly vertical side walls, i.e., the ablation profile was nearly perpendicular to the epoxy surface. Two improvements were developed to control the profile further.

First, a material with a greater ablation threshold than the epoxy was utilized to act as a hard stop to limit the ablation depth and ultimate post length (figure 3.A). Both silicon wafers and glass disks were evaluated; the glass disks exhibited better performance as a hard stop.

Second, sacrificial materials were introduced to absorb the portion of the ablation profile closest to the epoxy surface, which was much wider than the remainder of the ablated region (figure 3.B). A thick electrical tape (250 μm, 10 mils) was added to the ablation sample lay-up to absorb this energy. Wafer dicing tape (Semiconductor Equipment Corporation, medium tack) between the epoxy and the electrical tape assisted in removal upon pattern transcription. The final configuration for the laser ablation sample layup is shown in figure 3.C. A top-down view of an epoxy sample that was subjected to laser ablation patterning is shown in figure 3.D.

3.A Pillars replicated from laser ablation patterning thick epoxy coupons.

3.B Hypothetical ablation profile through epoxy matrix.

3.C Material stack-up for ablation of cylindrical holes in controlled thickness epoxy surfaces.

- Electrical Tape
- Dicing Tape
- Epoxy
- Adhesion Promoter
- Glass Substrate

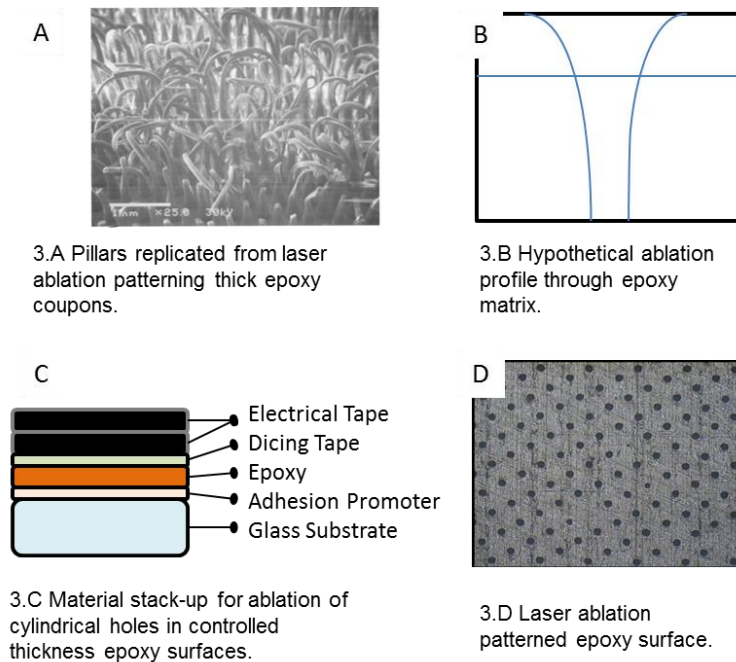3.D Laser ablation patterned epoxy surface.

Figure 3.   Development of fabrication scheme for laser ablation patterning of epoxy matrix masters.

3.2   Template Generation via Contact Lithography

Another method explored to generate a mask template was to use contact lithography (figure 4). Silicon wafers were prepared for this process by first removing any surface contaminants or residual organic materials by exposing them to a Radio Frequency (RF) oxygen plasma for 10 minutes. A dehydration-bake step was rapidly followed by an adhesion promotion surface chemical modification step. Various surface modification techniques were explored including application of molecular surface modifying agents that would chemically bond to the surface and vapor deposited copper. Next, a photoresist (SU-8 2050) was applied to the prepared silicon wafer using a syringe. This approach was utilized to prevent introduction of air bubbles into the photoresist which would cause catastrophic surface defects in the final sample. Once applied, the photoresist was spread using a spin coater with an initial spread cycle (500 rpm for 10–15 s) followed by a spin cycle (2500 rpm for 45 s). This ensured that, except for an edge bead which is a typical artifact of this deposition process, the photoresist coated the entire surface in a uniform layer that was approximately 50 μm thick.   The post-application bake was performed on a hot plate ramped from room temperature to 95 °C for 10 min followed by a 30-min hold. During the exposure process, direct contact between the photoresist and the photomask was extremely important for consistent pattern transcription. Early experiments were unsuccessful due to foreign particles and surface non-uniformities that prevented contact (figure 4.A). Careful handling of substrates in a clean environment and increased contact force applied using a vacuum chuck improved pattern transcription. Ultra-violet (UV) exposure was carried out with a broad band source through a long pass filter with a 350 nm cut-off. The exposure dose was estimated to be 200 mJ/cm^2 based on the total output of the illumination source and the area of the sample. The post-exposure bake was staged by alternating between two hotplates. The substrates were first baked at 65 °C for one minute, then 7 min at 95 °C, and then returned to 65

°C for one additional minute before cooling to room temperature (approximately 15 min). After cooling, substrates were immersed in propylene glycol monomethyl ether acetate (PGMEA) developer. The resultant master template consisted of a silicon wafer with approximately 50 μm of crosslinked SU-8 photoresist patterned with vias (figure 4.B). Molds were successfully prepared with via diameters down to 10 micrometers.

Interfacial stresses caused the cross-linked photoresist to delaminate from the surface of the wafer. To mitigate this, a new photomask was designed to generate a regular array of lines in the developed photoresist (figure 4.C). The trenches allowed the resist to strain slightly, thereby reducing the tensile stress generated in the photoresist during the post-exposure bake, resulting in a more stable film. Each of the nine large regions in figure 4.C contains a different feature size and pitch correlating with an ultimate difference in post diameter and spacing. Various line widths and pitches were also used to reduce stress in the films because the optimum trench design was not known. figure 4.D shows a higher magnification view of the region outlined in figure 4.C. Within each 2 mm square is an array of circular features that are approximately 10 μm in diameter separated by 60 μm.

4.A Cross-section micrograph of photoresist with incompletely transcribed vias. The vias do not penetrate to the wafer surface.

4.B Cross-section micrograph of photoresist with successfully transcribed vias. The vias penetrate to the wafer surface.

4.C Macroscopic view of designed photomask with large lines between patterned regions.

4.D Schematic of outlined region in 4.C indicating the smaller lines between regions.
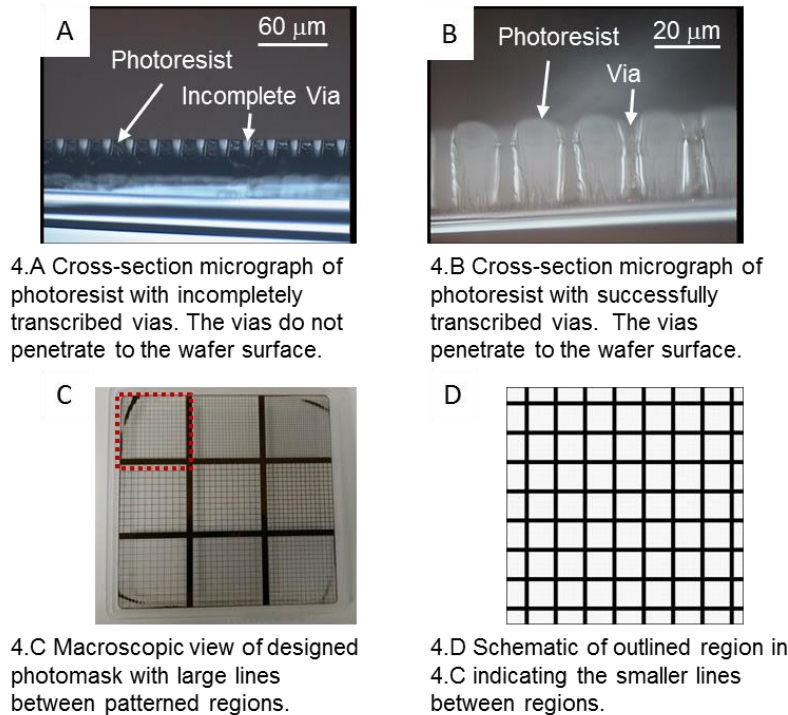
Figure 4. Refinement of contact lithographic approach for master generation is SU-8 photoresist.

3.3 Micropost Fabrication

3.3.1 *Silicone Evaluation*

Once the master templates were generated using either laser ablation patterning or contact lithography, the next step was to fabricate the micropost arrays using soft lithography. Several silicone-based materials were evaluated for micropost array generation. Each of the two-part silicones was mixed according to the manufacturers' instructions. A majority of the samples were generated using Silastic® T2 (Dow-Corning). This flexible, chemically inert, durable silicone is used for a myriad of applications and has excellent environmental durability properties. Additionally, as it is a two-part silicone, the ratio of the two components (typically 10 : 1 base : hardener) can be varied resulting in changes in the mechanical properties of the resultant material. Likewise, Sylgard® 184 (Dow-Corning) has also been used extensively and was evaluated in this work as a low elastic modulus alternative to Silastic® T2. To generate the micropost arrays from the master templates, the two part silicone was mixed and spread over the patterned region. This was placed in a vacuum chamber and held under reduced pressure for an hour to enable wetting of the topographical features and removal of trapped air pockets. The silicone was cured at 70 °C for approximately 4 hours and allowed to cool to room temperature before removal from the template. Using the initial epoxy templates with very deep holes, approximately 40 percent of the silicone microposts fractured upon removal from the template. Microposts closer to the desired length were usually readily separated from the template. Excellent silicone microposts were generated from templates prepared using either laser ablation (figure 5.A and B) or contact lithography (figure 5.C and D) when the templates had appropriately sized features in them.

5.A Microposts generated from laser ablation prepared master.

5.B Enlarged view of microposts in 5.A.

5.C Microposts generated from contact lithography prepared master.

5.D Enlarged view of microposts in 5.C.
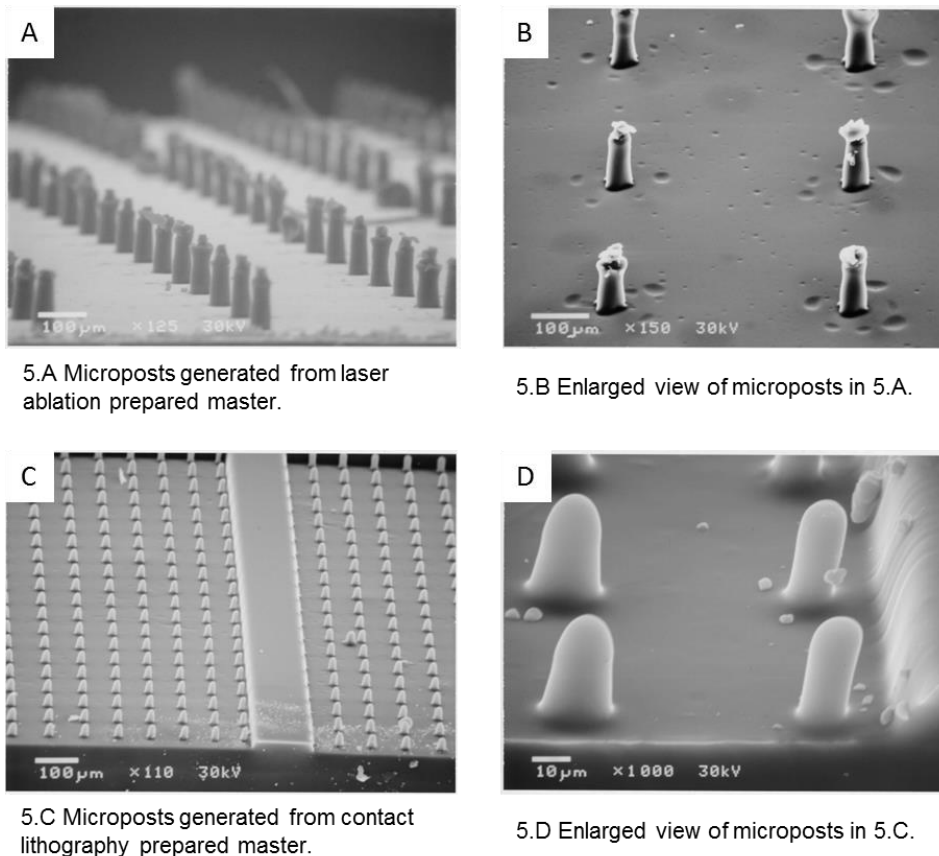
Figure 5.   Images of Silastic T2 microposts.

Several other silicone materials were evaluated (table 1). With the variation in modulus for these materials, from 0.06 MPa to 1.84 MPa, micropost arrays made from these materials would likely be applicable to a variety of wind speeds and flow conditions. For most of the materials evaluated, the microposts were readily removed from the templates and resulted in uniform arrays. However, the Sylgard 184 and Solaris A-15 both exhibited a propensity to tearing which made removal difficult. It is possible that changing the ratio of the silicone to hardener for these materials would alleviate these issues, but that was not investigated in this work.

Table 1. **Mechanical properties and post fabrication results for the silicone materials evaluated in this work.**

Silicone	Modulus, MPa	Tensile Strength, MPa	Micropost Fabrication
Sylgard 184[a]	1.84	7.07	✓[c]
Silastic T2[a]	1.50	5.52	✓
Moldstar 30[b]	0.66	2.90	✓
Solaris A-15[b]	0.17	1.24	x[c]
EcoFlex 0050[b]	0.08	2.14	✓
EcoFlex 0010[b]	0.06	0.83	✓

[a]Dow Corning
[b]Smooth-On, Inc.
[c]These silicones were brittle and difficult to work with for this application.

3.3.2 *Capping of Posts*

Our micropost design involves a "cap" on top of each post. This cap will enable greater deflection resolution by increasing the optical detection area and is anticipated to improve the sensitivity of the posts. Micropost caps were prepared by wetting the post tip with uncured silicone followed by cap shaping and silicone curing on a clean surface (figure 6).
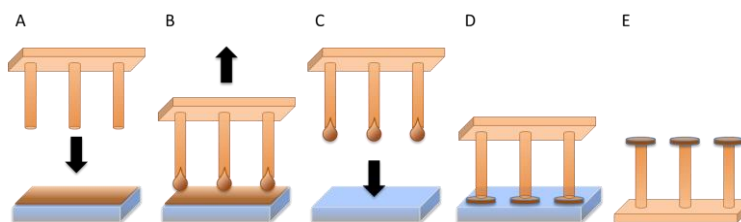

Figure 6. **Schematic for fabricating caps on the post tips. In this process, a micropost array is placed in contact with a glass substrate coated with a spin-coated uncured silicone layer (A). The micropost array is removed from this surface leaving microdroplets of uncured silicone on the post tips (B) and is brought into contact with a clean glass substrate (C). The uncured silicone partially wets the micropost and partially wets the substrate resulting in formation of circular structures (D) that, once cured, can be removed from the substrate remaining bound to the micropost tips (E).**

Thickness of the uncured silicone film was controlled by spin casting after calibration to prepare a spin curve. Figure 7.A shows a representative spin curve generated for Sylgard 184, which was chosen due to its reduced viscosity relative to Silastic T2. Using this information, proper surface preparation techniques could be performed to generate a Sylgard 184 coated surface with an appropriate thickness (5–15 µm). A supported silicone micropost array was carefully brought

into contact with the coated surface resulting in transfer of uncured Sylgard 184 material to the tips of the silicone microposts. The wetted microposts were next placed in contact with a clean surface resulting in spreading of the uncured silicone and formation of the micropost cap. While in contact with the clean surface, the capped microposts were placed in a 70 °C oven to cure the cap material. The resultant posts are shown below (figure 7.B).

3.3.3 *Fluorescent Caps*

To demonstrate the feasibility to filter the signals detected from the cap movement relative to reflection from the substrate, Silastic T2 was doped with rhodamine B, a fluorescent laser dye. Upon illumination with a UV light source, the fluorescent emission from the doped silicone was readily visible on our macroscopic post sample (figure 7.C). This approach will be used to improve signal to noise ratios in actual sensor systems and is amenable to using excitation sources commonly available in wind tunnels (i.e., Nd:YAG lasers, $\lambda = 532$ nm).
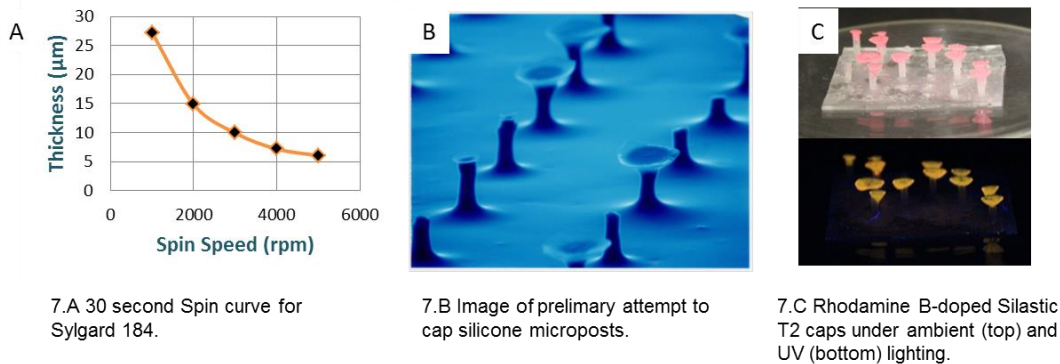
7.A 30 second Spin curve for Sylgard 184.

7.B Image of prelimary attempt to cap silicone microposts.

7.C Rhodamine B-doped Silastic T2 caps under ambient (top) and UV (bottom) lighting.

Figure 7.   Generation of "capped" microposts.

3.4   Mechanical Characterization of Micropost Deflection

Once micropost arrays were repeatedly fabricated, experiments were conducted to characterize the mechanical properties of the microposts using atomic force microscopy (AFM). Based on existing literature, three techniques were investigated for this non-traditional use of AFM equipment. One technique involving contact mode scanning of a post-decorated surface was quickly excluded as the target heights of the post were too great for this approach to be viable (Ref. 26). The other two techniques collect force/displacement curves on the posts as they are bent by the AFM cantilever. Although somewhat similar, one technique involved bending the cantilever down by placing the post on top of the cantilever (Ref. 27), and the other technique involved bending the post down by moving the cantilever in that direction (Ref. 28). Ultimately, the last technique was chosen due to the instrumentation available. For these measurements, a Veeco Digital Instruments Multimode Scanning Probe Microscope with a Nanoscope V Controller was used. The probes used were MicroMasch cantilevers, CSC12 Tip E with an aluminum coated detector side. The manufacturer data indicated that the average spring constant was $k = 0.03$ N/m. For this technique, cantilevers acquired previously were first calibrated to determine an accurate spring constant. This was achieved by determining fundamental vibrational frequencies for three vibrational modes (bending, lateral, and torsional) using an

oscilloscope (Ref. 29). Next, the cantilever was placed in contact with the post at a determined distance from the base (figure 8.A, points 1, 2 and 3) and translated down to deflect the post. The deflection of the cantilever was used to calculate the requisite force for post deflection using Hooke's Law. Figure 8 shows an example of a post that was interrogated using this technique. Figure 8.B–D show the orientation of the cantilever at three different positions on the post prior to post bending.
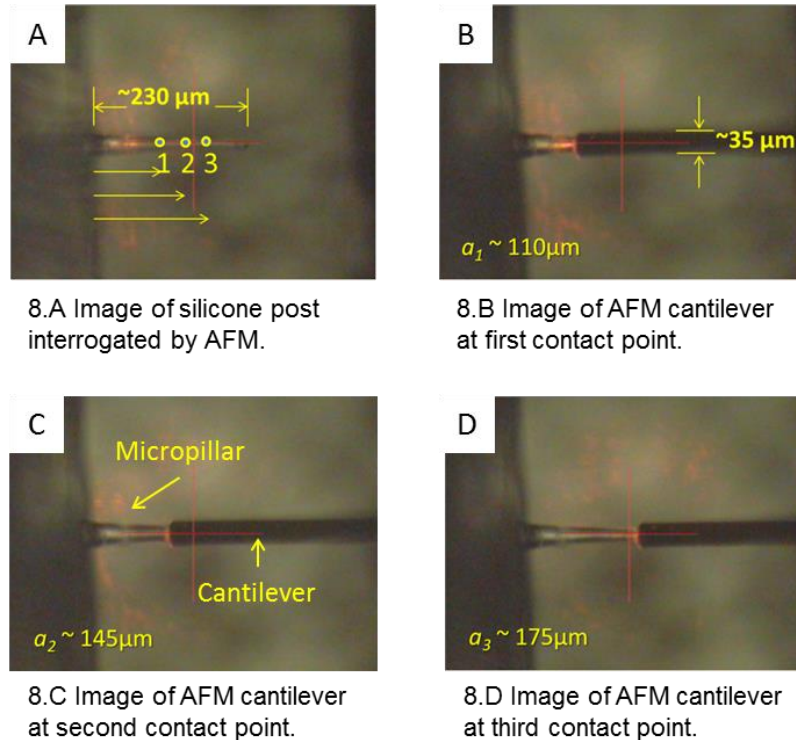

8.A Image of silicone post interrogated by AFM.

8.B Image of AFM cantilever at first contact point.

8.C Image of AFM cantilever at second contact point.

8.D Image of AFM cantilever at third contact point.

Figure 8.   Micropost deflection using AFM.

Figure 9.A reports an example of the data collected on the post shown in figure 8. As the cantilever was translated downward, it first contacted the micropost. Further movement of the cantilever, resulting in post bending, required additional force. This additional force was recorded as the deflection force in figure 9.A. The deflection force was greater as the cantilever was brought closer to the post base, as would be anticipated. Initially, the load measured at all three test locations was collinear which was attributed to the embedding of the cantilever tip into the silicone post. This can be avoided by using tipless cantilevers. Although not pursued in the efforts described here, a model describing the required force to embed the AFM tip into an elastomeric post is available and the experimentally measured deflection force can be corrected accordingly (Ref. 30). Deflection of the AFM cantilever arising from post deflection likely initiated where the three traces separate according to the cantilever position, which occurs at approximately 0.6 μm.

9.A Force deflection curve measured on the micropillar in fig 8.

9.B Schematic of the change in airflow velocity along the micropillar profile with a no-slip condition.
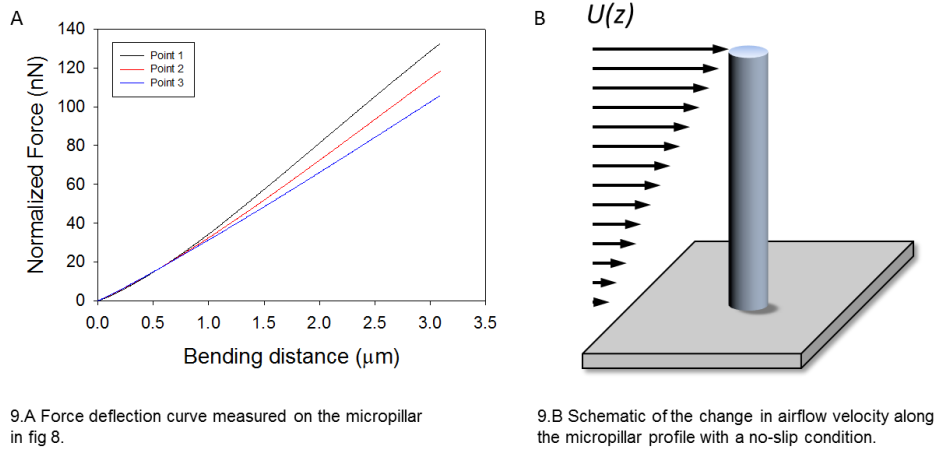
Figure 9. AFM micropost deflection results and a schematic of airflow interactions with a micropost.

3.5 Measurement Capability

Deflection of the micropost shear stress sensor components might be visualized using existing wind tunnel technologies involved with particle image velocimetry (PIV), specifically μ-PIV systems (Ref. 31). Using state-of-the-art μ-PIV systems, imaging at micrometer per pixel levels and lower is achievable. Thus, a 100 μm post with a deflection of 10 μm should have a change in position of at least 10 pixels in a single direction. A 20 μm diameter post with a 50 μm "cap" would occupy 2032 pixels. With the large "caps" resolutions, much better than 0.01 pixels should be achievable corresponding to a maximum number of data points approaching 1000 or more.

To calculate shear sensitivity, deflection forces measured using the AFM technique were equated to drag forces experienced by a micropost in a fluid flow using the Oseen approximation (Ref. 32, 33). See 1.1.1.Appendix A for a description of this calculation. Based on the AFM experiments, a 3 μm deflection (the maximum travel range of the instrument) was approximately a 1.2 percent deflection relative to the post length (175 μm), equating to a shear stress of approximately 820 mPa (table 2). An extrapolation of the post deflection to 10 percent would develop a force of 0.58 μN (Appendix A). Using the relationship between drag force and shear stress described in Appendix A, the shear stress created by the flow would be approximately 3 Pa (see eq. (A.3)) assuming that the change in velocity is equal to twice the average velocity as would be the case for no-slip boundary conditions (Figure A.3). Thus, these microposts, fabricated from commercially available materials, would potentially enable the determination of shear stresses present in subsonic turbulent flows.

Table 2. **Post deflection and force as determined from AFM measurements with the equivalent shear stress necessary to cause such deflection calculated according to 1.1.1.Appendix A.**

Post Deflection (µm)	Force (nN)	τ (mPa)
2.9	100	823
1.6	50	517
0.4	10	176
0.2	5	112

Section 4. **Summary**

In this work, elastic micropillars were designed to meet anticipated limitations within a wind tunnel environment to minimize disruption of the airflow. A model was used to calculate the profile drag force necessary to deflect a cantilever beam defined by Euler-Bernoulli beam theory. From this result, both photolithography and laser ablation patterning were evaluated as approaches to generate templates. Soft lithography was used to replicate silicone substrates with sensing elements from these templates. The efficacy of capping the pillar tips was evaluated using a straightforward tip wetting approach. In a maco-scale demonstration, fluorescent dye improved pillar tip contrast relative to the substrate surface for enhanced detection. AFM was used to quantitatively determine deflection forces which were correlated with drag forces experienced by a micropost in a fluid flow.

Section 5. **Outlook**

The current TRL of this micropost sensor technology is estimated to be 2–3 (Ref. 34). Before implementing these micropost arrays as sensors in a wind tunnel experiment, the repeatability of micropost fabrication needs to be verified, post deflection in a known shear field environment needs to be performed and post deflection needs to be related to the AFM results. Beyond this, the sensor bandwidth, frequency response, noise floor, multipost-airflow interactions, etc. will determine their utility as sensors. The micropost frequency response range and fundamental frequencies can be determined using simple cantilever deflection calculations and verified using deflection experiments and high speed imaging. Deformation of the post caps and changes in response to shear stress as a result of deflection of the capped post could be addressed in programming platforms such as COMSOL.

Section 5. **References**

1.   Dijkstra, M.; van Baar, J. J.; Wiegerink, R. J.; Lammerink, T. S. J.; de Boer, J. H.; Krijnen, G. J. M., Artificial Sensory Hairs Based on the Flow Sensitive Receptor Hairs of Crickets. *J. Micromech. Microeng.* **2005,** *15*, S132-S138.

2.   Naughton, J. W.; Sheplak, M., Modern developments in shear-stress measurement. *Prog. Aerospace Sci.* **2002,** *38*, 515-570.

3.   Lofdahl, L.; Gad-el-Hak, M., MEMS-Based Pressure and Shear Sensors for Turbulent Flows. *Meas. Sci. Technol.* **1999,** *10* (8), 665-686.

4.   Meloy, J.; Griffin, J.; Sells, J.; Chandrasekaran, V.; Cattafesta, L.; Sheplak, M., Experimental Verification of a MEMS Based Skin Friction Sensor for Quantitative Wall Shear Stress Measurement. In *41st AIAA Fluid Dynamics Conference and Exhibit*, Honolulu, Hawaii, 2011.

5.   Ioppolo, T.; Ayaz, U. K.; Otugen, M. V., Performance of a Micro-Optical Wall Shear Stress Sensor Based on Whispering Gallery Mode Resonators. In *47th AIAA Aerospace Sciences Meeting*, American Institute of Aeronautics and Astronautics, Inc.: Orlando, FL, 2009.

6.   Brucker, C.; Spatz, J.; Schroder, W., Feasability Study of Wall Shear Stress Imaging using Microstructured Surfaces wuth Flexible Micropillars. *Exp. Fluids* **2005,** *39*, 464-474.

7.   Grobe, S.; Schroder, W.; Brucker, C., Nano-Newton Drag Sensor Based on Flexible Micro-Pillars. *Meas. Sci. Technol.* **2006,** *17*, 2689-2697.

8.   Schmitz, G. J.; Brucker, C.; Jacobs, P., Manufacture of High-Aspect-Ratio Micro-Hair Sensor Arrays. *J. Micromech. Microeng.* **2005,** *15*, 1904-1910.

9.   Grobe, S.; Schroder, W., Mean Wall-Shear Stress Measurements Using the Micropillar Shear-Stress Sensor MPS3. *Meas. Sci. Technol.* **2008,** *19*, 015403.

10.   Grobe, S.; Schroder, W., Dynamic Wall-Shear Stress Measurements in Turbulent Pipe Flow Using Micro-Pillar Sensors MPS3. *Int. J. Heat Fluid Flow* **2008,** *29*, 830-840.

11.   Notterbrock, B.; Klaas, M.; Schroder, W., Improvement of the Measurement Range of the Micro-Pillar Shear-Stress Sensor MPS3. In *28th AIAA Aerodynamic Measurement Technology, Ground Testing, and Flight Testing Conference*, New Orleans, Louisiana, 2012.

12.   Autumn, K.; Liang, Y. A.; Hsieh, S. T.; Zesch, W.; Chan, W. P.; Kenny, T. W.; Fearing, R.; Full, R. J., Adhesive Force of a Single Gecko Foot-Hair. *Nature* **2000,** *405*, 681-685.

13.   Geim, A. K.; Dubonos, S. V.; Grigorieva, I. V.; Novoselov, K. S.; Zhukov, A. A.; Shapoval, S. Y., Microfabricated Adhesive Mimicking Gecko Foot-Hair. *Nat. Mat.* **2003,** *2*, 461-463.

14.   Tuteja, A.; Choi, W.; Ma, M.; Mabry, J. M.; Mazzella, S. A.; Rutledge, G. C.; McKinley, G. H.; Cohen, R. E., Designing Superoleophobic Surfaces. *Science* **2007,** *318*, 1618-1622.

15.   Callies, M.; Chen, Y.; Marty, F.; Pepin, A.; Quere, D., Microfabricated textured surfaces for superhydrophobic investigations. *Microelectron. Eng.* **2005,** *78-79*, 100 - 105.

16.   Oner, D.; McCarthy, T. J., Ultrahydrophobic surfaces. Effects of topography length scales and wettability. *Langmuir* **2000,** *16*, 7777 - 7782.

17.   del Campo, A.; Greiner, C.; Arzt, E., Contact shape controls adhesion of bioinspired fibrillar surfaces. *Langmuir* **2007,** *23*, 10235 - 10243.

18.   Rajput, D.; Costa, L.; Lansford, K.; Terekhov, A.; Hofmeister, W., Solution-Cast High-Aspect-Ratio Polymer Structures from Direct-Write Templates. *ACS Appl. Mater. Interfaces* **2013,** *5*, 1-5.

19.   Gnanamanickam, E. P.; Sullivan, J. P., Manufacture of High Aspect Ratio Micro-Pillar Wall Shear Stress Sensor Arrays. *J. Micromech. Microeng.* **2012,** *22*, 125015.

20.   Kapadia, R.; Ko, H.; Chueh, Y.-L.; Ho, J. C.; Takahashi, T.; Zhang, Z.; Javey, A., Hybrid Core-Multishell Nanowire Forests for Electrical Connector Applications. *App. Phys. Lett.* **2009,** *94*, 263110.

21.   Chandra, D.; Yang, S., Stability of High-Aspect-Ratio Micropillar Arrays against Adhesive and Capillary Forces. *Acc. Chem. Res.* **2010,** *43* (8), 1080-1091.

22.   Grobe, S.; Schroder, W., The Micro-Pillar Shear-Stress Sensor MPS3 for Turbulent Flow. *Sensors* **2009,** *9*, 2222-2251.

23.   Schneider, F.; Fellner, T.; Wilde, J.; Wallrabe, U., Mechanical Properties of Silicones for MEMS. *J. Micromech. Microeng.* **2008,** *18*, 065008.

24.   Belcher, M.; Wohl, C.; Hopkins, J.; Connell, J., Laser Surface Preparation for Bonding of Aerospace Composites. *Eng. Comput. Mech.* **2011,** *164* (3), 133-138.

25.   Wohl, C. J.; Belcher, M. A.; Chen, L.; Connell, J. W., Laser Ablative Patterning of Copoly(imide siloxane)s Generating Superhydrophobic Surfaces. *Langmuir* **2010,** *26* (13), 11469-11478.

26.   Song, J.; Wang, X.; Riedo, E.; Wang, Z., Elastic Property of Vertically Aligned Nanowires. *Nano Lett.* **2005,** *5* (10), 1954-1958.

27.   Kallesoe, C.; Larsen, M. B.; Boggild, P.; Molhave, K., 3D Mechanical Measurements with an Atomic Force Microscope on 1D Structures. *Rev. Sci. Instrum.* **2012,** *83*, 023704.

28.   Gordon, M. J.; Baron, T.; Dhalluin, F.; Gentile, P.; Ferret, P., Size Effects in Mechanical Deformation and Fracture of Cantilevered Silicon Nanowires. *Nano Lett.* **2009,** *9* (2), 525-529.

29.   McFarland, A. W.; Poggi, M. A.; Bottomley, L. A.; Colton, J. S., Characterization of microcantilevers solely by frequency response acquisition. *J. Micromech. Microeng.* **2005,** *15*, 785-791.

30.   Cheng, Y.-T.; Cheng, C.-M., Scaling, dimensional analysis, and indentation measurements. *Mat. Sci. Eng. R* **2004,** *44*, 91-149.

31.   Raffel, M.; Willert, C.; Kompenhans, J., *Particle Image Velocimetry: A Practical Guide (Experimental Fluid Mechanics)*. 2nd Edition ed.; Springer: Berlin, Germany, 2007; p 448.

32.   Deen, W., M., *Analysis of Transport Phenomena*. Gubbins, K. E., Ed. New York, 1998; p 597.

33.   Wiesenborn, A. J.; Mazur, P., The Oseen Drag on a Circular Cylinder Revisited. *Phys. A: Stat. Mech. App.* **1984,** *123* (1), 191-208.

34.   Sanchez, R. DOE G 413.3-4A, Technology Readiness Assessment Guide. 2001,

Appendix A. Approximation of Shear Stress on a Surface Based on AFM Derived Forces of a PDMS Micropost

An approximate relationship between the force imparted on a pillar surface in a flow and the shear stress induced by the same flow is presented here. The model equates the drag forces induced on a pillar with experimental load/displacement data from the mechanical testing of a single pillar. This derivation is intended to show that a typical boundary layer flow can reasonably be expected to cause deflection of the micropost tips using an approximate analysis. A full fluid dynamic and material elastic model of flow interaction with a micropost is beyond the scope of this effort. The free stream properties are calculated from the drag force using experimental data obtained from Stokes flow around an infinite cyclinder. The data provided by Weizenbron and Mazur (ref. 33) relate the drag coefficient (C_D) to the Reynolds number (Re) for low values of Re. The method described results in approximate values to help guide the selection of pillar geometries and materials that will result in deflection.

The force to bend a micropost such that the free end is displaced by 3 μm was measured by AFM, as described in this report. The force required to deflect the free end to 10 percent of the post height is extrapolated using elastic beam theory to obtain the maximum allowable load on a micropost for shear stress measurement as described in section 2. The extrapolated point force applied by the AFM is approximately equal to a flow induced drag force acting on a post of the same dimensions. An order of magnitude approximation can be made by assuming the post behaves as an infinitely long cylinder and is in a uniform Stokes flow (figure a.1). The velocity of the flow field far from the cylinder can be calculated from the drag equation which accounts for skin friction and form drag. Using this velocity, the average velocity in a flow field near a surface can be estimated from the definition of Newtonian shear stress.
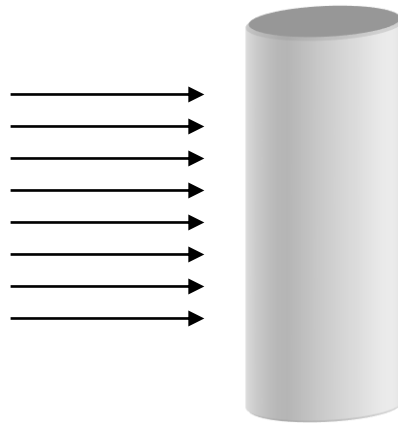

Figure A.1. Schematic of velocity vectors acting on an infinite cylinder in a Stokes flow.

Elastic beam theory can be used to accurately model tip deflection up to 10% of the beam length. Using 10% of the pillar height as the tip deflection limit, the load of 583 nN was used in the drag equation (eq. (A.1)) as the drag force.

Table A.1 shows the experimental values used from the micropost bending experiment and the extrapolated values at 10% tip deflection.

Table A.1. **Comparison of experimental data and the extrapolated values for tip deflection equal to 10% of the post height.**

Parameter	Experimental Data	Extrapolation Value
Post Length (µm)	175	175
Tip Deflection (µm)	3	17.5
Tip Defection as % of Height	1.7	10
Load (nN)	105	613

The drag force given by equation (A.1) is related to the free stream fluid velocity (v)

$$F_D = \frac{1}{2}\rho v^2 C_D A$$

(A.1)

where the density (ρ), the drag coefficient (C_D), and the frontal area of a post (A) are constants that are known for a given flow and bluff body geometry. The drag coefficient for an infinite, circular cylinder in Stokes flow is Re dependent and is shown in Figure A.2 as the solid black curve. The solid line from fig. A.2 was digitized and fit with a power law function given by equation (A.2).

$$C_D = 7.61 Re^{-0.48}$$

(A.2)

where Re is the Reynolds number of the flow around the micropost. The Re is determined from v and known constants: ρ, the diameter of a micropost (d = 20 µm), and the viscosity of air (μ = 18.2 µPa s). The power law fit to the digitized data was quite good with an R^2 value of 0.98. Expressing the Re in terms of v and substituting equation (A.2) into equation (A.1), the relationship between v and F_D is give by equation (A.3).

$$v = 0.415 \left(\frac{F_D}{\rho A}\right)^{0.658} \left(\frac{\mu}{\rho d}\right)^{-0.316}$$
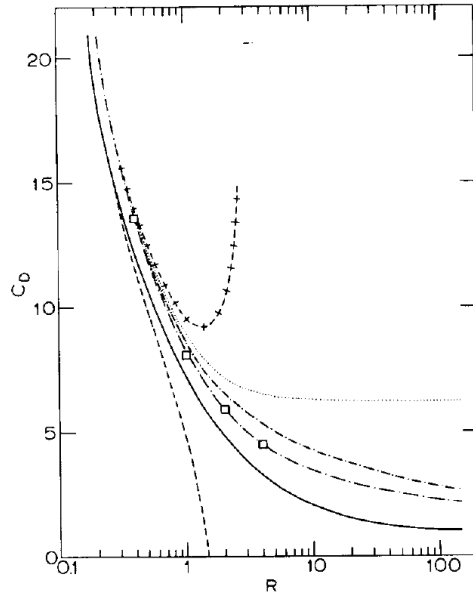
(A.3)

Figure A.2. Coefficient of drag for an infinite cylinder in Stokes flow. The solid line represents experimental data. Other curves are generated for analytical approximations. Copied from reference 33.

The shear stress imparted on a surface by a flowing Newtonian fluid is defined as

$$\tau = \mu \frac{\delta v}{\delta z} \tag{A.4}$$

where τ is the shear stress, μ is the dynamic viscosity, and z is the distance from the surface. For this approximation, the velocity of a uniform flow field past an infinite cylinder (v), as calculated from equation A.4, is assumed to equal the average velocity of the gradient flow field in the boundary layer above a surface (v_{avg}). Figure A.3 below represents this graphically.

$$v = v_{avg}$$
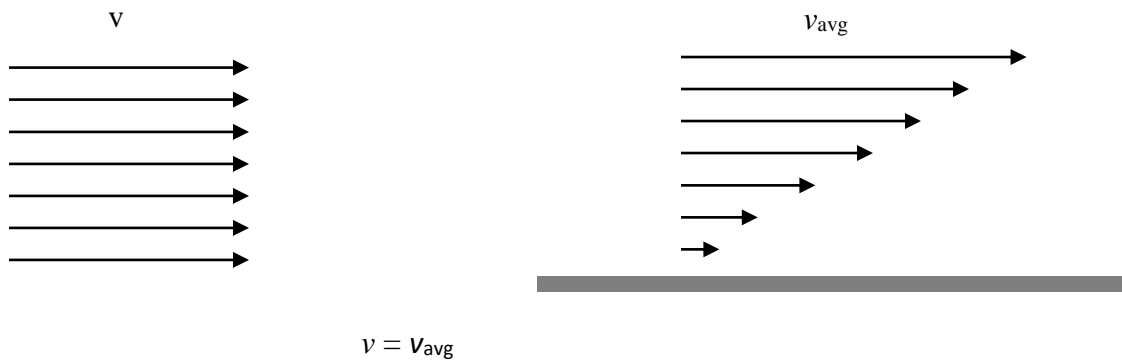
Figure A.3. Schematic of the change in the velocity profile from the free stream, left, to that in the boundary layer with a no-slip condition, right.

Using this assumption and knowledge that velocity of the flow varies linearly within the viscous sublayer, the resulting shear stress on a flat surface can be determined from equation (A.5):

22

$$\tau = \mu \frac{\Delta v}{\Delta z}$$

$$(A.5)$$

where the change in velocity (Δv) is twice the v_{avg} and the change in height (Δz) is the length of the post, l. Therefore, the shear stress can be determined by combining equations (A.4) and (A.5) to yield):

$$\tau = 0.93 \frac{\mu}{l} \left(\frac{F_D}{\rho A} \right)^{0.658} \left(\frac{\mu}{\rho d} \right)^{-0.316}$$

$$(A.6)$$

Equation (A.6) is an approximate calibration function for relating the force to deflect the tip of a micropost to shear stress on a smooth surface. Using the relationship between F_D and tip deflection presented in table (A.1), a calibration curve can be drawn between shear stress and percent tip deflection as shown in Figure (A.4).
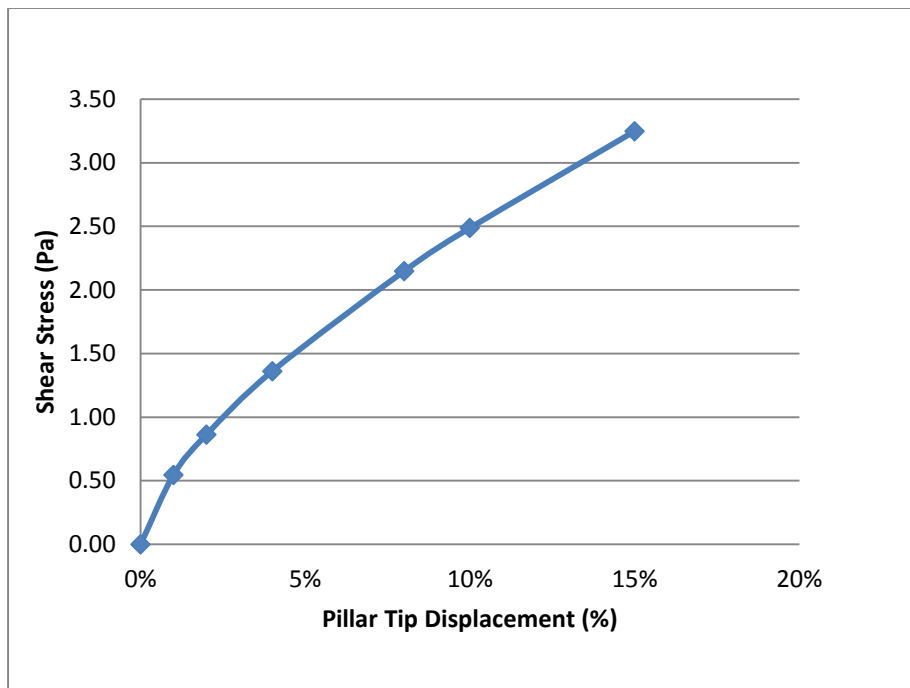

Figure A.4.   An approximate calibration curve relating shear stress on a smooth surface to the percentage of tip displacement (relative to micropost length).

REPORT DOCUMENTATION PAGE

1. REPORT DATE (DD-MM-YYYY)	2. REPORT TYPE	3. DATES COVERED (From - To)
01-12-2015	Technical Publication	

4. TITLE AND SUBTITLE

Flexible Micropost Arrays for Shear Stress Management

5a. CONTRACT NUMBER

5b. GRANT NUMBER

5c. PROGRAM ELEMENT NUMBER

6. AUTHOR(S)

Wohl, Christopher J.; Palmeieri, Frank L.; Hopkins, John W.; Jackson, Allen M.; Connell, John W.; Lin, Yi; Cisotto, Alexxandra A.

5d. PROJECT NUMBER

5e. TASK NUMBER

5f. WORK UNIT NUMBER

694478.02.93.02.12.34.23

7. PERFORMING ORGANIZATION NAME(S) AND ADDRESS(ES)

NASA Langley Research Center
Hampton, VA 23681-2199

8. PERFORMING ORGANIZATION REPORT NUMBER

L-20646

9. SPONSORING/MONITORING AGENCY NAME(S) AND ADDRESS(ES)

National Aeronautics and Space Administration
Washington, DC 20546-0001

10. SPONSOR/MONITOR'S ACRONYM(S)

NASA

11. SPONSOR/MONITOR'S REPORT NUMBER(S)

NASA/TP-2015-21896

12. DISTRIBUTION/AVAILABILITY STATEMENT

Unclassified - Unlimited
Subject Category 27
Availability: STI Program (757) 864-9658

13. SUPPLEMENTARY NOTES

14. ABSTRACT

Increased fuel costs, heightened environmental protection requirements, and noise abatement continue to place drag reduction at the forefront of aerospace research priorities. Unfortunately, shortfalls still exist in the fundamental understanding of boundary-layer airflow over aerodynamic surfaces, especially regarding drag arising from skin friction. For example, there is insufficient availability of instrumentation to adequately characterize complex flows with strong pressure gradients, heat transfer, wall mass flux, three-dimensionality, separation, shock waves, and transient phenomena. One example is the acoustic liner efficacy on aircraft engine nacelle walls. Active measurement of shear stress in boundary layer airflow would enable a better understanding of how aircraft structure and flight dynamics affect skin friction. Current shear stress measurement techniques suffer from reliability, complexity, and airflow disruption, thereby compromising resultant shear stress data. The state-of-the-art for shear stress sensing uses indirect or direct measurement techniques. Indirect measurements (e.g., hot-wire, heat flux gages, oil interferometry, laser Doppler anemometry, small scale pressure drag surfaces, i.e., fences) require intricate knowledge of the studied flow, restrictive instrument arrangements, large surface areas, flow disruption, or seeding material; with smaller, higher bandwidth probes under development.

15. SUBJECT TERMS

Boundary layer; Elastomer; Micropillar; Shear stress

16. SECURITY CLASSIFICATION OF:			17. LIMITATION OF ABSTRACT	18. NUMBER OF PAGES	19a. NAME OF RESPONSIBLE PERSON
a. REPORT	b. ABSTRACT	c. THIS PAGE			STI Help Desk (email: help@sti.nasa.gov)
U	U	U	UU	33	19b. TELEPHONE NUMBER (Include area code)
					(443) 757-5802